Global Semi-Lagrangian Atmospheric Model Based on Compact Finite-Differences and its Implementation on a Parallel Computer

Mikhail Tolstykh

HAL Id: inria-00073612
https://inria.hal.science/inria-00073612

Submitted on 24 May 2006

Global semi-Lagrangian atmospheric model based on compact finite-differences and its implementation on a parallel computer

Mikhail Tolstykh

N˙ **3080**

January 1997

———— THÈME 4 ————

_R_ _apport_
de recherche

Global semi-Lagrangian atmospheric model based on compact finite-differences and its implementation on a parallel computer

Mikhail Tolstykh*

Abstract: The semi-Lagrangian atmospheric model on the sphere based on compact finite differences is presented. In the two-dimensional case, the potential vorticity is used as one of the prognostic variables. Fourth-order compact finite differences are used to discretize first- and second-order derivatives. The results including real data tests presented for 2D shallow water version with orography demonstrate its accuracy with the time steps several times greater than in Eulerian model. The 3D version of the model uses the absolute vorticity equation. Some results including a real data forecast are presented. The parallel implementation of the 3D model on a distributed memory parallel computer is described.

Key-words: Climate modelling, semi-Lagrangian scheme, compact finite-differences, parallel computing

(Résumé : tsvp)

Permanent affiliation: Institute of Numerical Mathematics, Russian Academy of Sciences, Moscow RUSSIA

* email: tolstykh@inm.ras.ru

Le modèle atmosphérique globale semi-Lagrangien basé sur les differénces compactes finies et son implantation sur l'ordinateur parallèle

Résumé : Le modèle de circulation atmosphérique globale 3D pour simulation de climat et les etudes des prédictabilité etait développé. Le vorticité est utilisé comme le variable pronostique. Le modèle est basé sur le schéma semi-Lagrangien que permette d'utiliser le pas de temps 3-4 fois plus que dans le schéma Eulérien. On a utilisé la version 2D sur la sphère pour développer le schéma numérique semi-implicite semi-Lagrangien en utilisant les différences compactes finies de 4ième ordre. Afin d'évaluer la précision du schéma semi-Lagrangien par rapport à un modèle de référence Eulérien spectral, on a fait les tests avec des données réelles. Les résultats montrent que le modèle donne le même niveau d'erreurs que le modèle de référence. Du point de vue numérique, la version 3D est une extension du modèle "shallow water" où on utilise la transformation diagonalisée des modes propres verticaux en ajoutant les équations de température et d' humidité. Les premiers résultats pour la version 3D sont présentés. Le modèle est parallélisé en utilisant la conception de mémoire distribuée avec l'aide de MPI (Message Passing Interface). Deux strategies de parallélization des calculs semi-Lagrangiens et leur résultats sont comparés.

Mots-clé : Modèlisation de climat, schéma semi-Lagrangien, différénces compactes finies, calculs paralleles

1   Introduction

Climate modelling is one of the most computer time-consuming problems in geoscience. While semi-Lagrangian approach (also known as backward characteristics method) allows to use greater time steps than permitted by CFL number it lacks the formal conservation properties. The potential vorticity is the global invariant of the atmospheric flow, so while discretizing its conservation law, one can achieve better conservation properties. This feature is of great importance for long-term integration of the model needed for predictability studies and simulation of climate. Semi-Lagrangian method is widely used now for numerical weather prediction but we see only few attempts to use it in climate modelling [3], [24] .

The approach based on semi-Lagrangian advection of potential vorticity was already applied in [4] for 2D model and has shown good results. In this case, the wind field is expressed in terms of a stream function and velocity potential. This also allows to use an unstaggered grid with a single set of trajectories for all variables thus avoiding multiple set of trajectories or additional interpolations associated with a staggered grid [4].

In the semi-Lagrangian models, the advection part is discretized with the fourth order. The finite-difference discretizations in the semi-implicit part of the model are usually of the second order. The compact finite differences used in this study allow to have the fourth-order discretization in the semi-implicit part thus giving overall fourth-order accuracy while retaining the simplicity of the second-order solvers. This is achieved by using the Fourier representation in the longitudinal direction. The latter also facilitates the implementation of the fourth-order implicit horizontal diffusion.

In this paper, we present the global finite-difference model which is based on the potential vorticity equation in the 2D case and absolute vorticity equation in the 3D case. The numerical results are given for both versions of the model. The parallel implementation of the 3D model on a distributed memory computer is described.

2   Formulation of the shallow-water model

The base shallow water equations on the sphere are potential vorticity equation

$$\frac{d}{dt}\left(\frac{\zeta + f}{\Phi - \Phi_s}\right) = 0,$$

momentum equations written in the vector form on the sphere

$$\left(\frac{d\mathbf{V}}{dt}\right)_H = -\nabla\Phi - f\mathbf{k} \times \mathbf{V}$$

and continuity equation

$$\frac{d(\Phi - \Phi_s)}{dt} = -(\Phi - \Phi_s)D.$$

Here ζ is the relative vorticity, Φ is the *atmosphere thickness*, Φ_s is the height of the surface, f - the Coriolis parameter, $\mathbf{V}$ - horizontal velocity, D - divergence, d/dt - three-dimensional Lagrangian derivative,

$$\left(\frac{d\mathbf{V}}{dt}\right)_H = \text{horizontal projection of} \quad \left(\frac{d\mathbf{V}}{dt}\right),$$

$$\nabla = \frac{\mathbf{i}}{a \cos \varphi} \frac{\partial}{\partial \lambda} + \frac{\mathbf{j}}{a} \frac{\partial}{\partial \varphi}$$

is gradient operator on the sphere, λ - longitude, φ - latitude, $\mathbf{V}$ is the vector of horizontal velocity with the components u and v in λ and φ directions respectively, a - the Earth radius and $\mathbf{k}$ is the unit vector in the vertical.

Momentum equations are used only to obtain the right hand side for the divergence equation.

A completely nonlinear discretization of governing equations was used in [4]. Our formulation combines that of [5] without divergence damping and the potential vorticity equation discretized in a simpler way than in [4] still leading to stable scheme. This means that we can use linear solver instead of nonlinear multigrid solver thus making the 3D model development easier.

The temporal discretization is based on the two-time level scheme with the extrapolation of nonlinear term in the continuity equation to the midpoint of the trajectory and linearized treatment of fast gravity waves (semi-implicit scheme) leading to Helmholtz-type equation to be solved at each time step. We use temporal uncentering in the momentum and continuity equations while using centered in time scheme for potential vorticity equation. The reason of uncentering is the suppression of the spurious orographic resonance intrinsic to the semi-Lagrangian models [19]

The discretization of the governing equations looks as follows (asterisk denotes the values at the departure points of trajectories):

Potential vorticity equation:

$$\left(\frac{\zeta + f}{\tilde{\Phi} - \Phi_s} \right)^{n+1} = \left(\frac{\zeta}{\Phi - \Phi_s} \right)_*^n + \left(\frac{1}{\Phi^n - \Phi_s} \right)_* f_*, \tag{1}$$

where

$$\tilde{\Phi}^{n+1} = \Phi_s + \left(\Phi^n - \Phi_s \right)_* \frac{1 - \frac{\Delta t}{2} D_*^n}{1 + \frac{\Delta t}{2} D^{n+1}}, \tag{2}$$

Momentum equations:

$$\left(\frac{\mathbf{V}^{n+1} - \mathbf{V}^n}{\Delta t} \right)_H = -\left(\frac{1 + \epsilon}{2} \left(\nabla \Phi + f \mathbf{k} \times \mathbf{V} \right)^{n+1} + \frac{1 - \epsilon}{2} \left(\nabla \Phi + f \mathbf{k} \times \mathbf{V} \right)_*^n \right).$$

Here ϵ is small first-order decentering parameter.

Continuity equation:

$$\frac{(\Phi'^{n+1} - \Phi_s) - (\Phi'^n - \Phi_s)_*}{\Delta t} = -\bar{\Phi} \left(\frac{1 + \epsilon}{2} D^{n+1} + \frac{1 - \epsilon}{2} D_*^n \right) - \left((\Phi' - \Phi_s) D \right)_M^{n+1/2}, \tag{3}$$

where $\Phi' = \Phi - \bar{\Phi}$, $\bar{\Phi}$ is the reference height, M denotes the values interpolated at the midpoint of trajectory. The values at the intermediate time level $n + 1/2$ for some function p are obtained from usual extrapolation $p^{n+1/2} = 3/2 p^n - 1/2 p^{n-1}$. Such extrapolation is also used to obtain the velocity components at time $n + 1/2$ necessary to find departure points.

We combine momentum equations to obtain the divergence equation:

$$D^{n+1} = -\frac{1 + \epsilon}{2} \Delta t \mathcal{L} \left(\Phi' \right)^{n+1} + \tilde{A}, \tag{4}$$

where the operator $\mathcal{L}$ is

$$\mathcal{L} = \frac{g}{a^2 \cos^2 \varphi} \frac{\partial^2}{\partial \lambda^2} - \frac{1}{a^2 \cos \varphi} \frac{\partial(gF)}{\partial \varphi} \frac{\partial}{\partial \lambda} + \frac{1}{a^2 \cos \varphi} \frac{\partial}{\partial \varphi} \left(g \cos \varphi \frac{\partial}{\partial \varphi} \right)$$

and

$$\tilde{A} = \frac{1}{a \cos \varphi} \left(\frac{\partial}{\partial \lambda} \Big[g \big(A_\lambda + F A_\varphi \big) \Big] + \frac{\partial}{\partial \varphi} \Big[g \cos \varphi \big(A_\varphi - F A_\lambda \big) \Big] \right),$$

$$F \;=\; \frac{1+\epsilon}{2} f \triangle t, \qquad g \;=\; (1 + F^2)^{-1},$$

$$A_\lambda = \alpha_1 R_{*\lambda}^{\,n} + \alpha_2 R_{*\varphi}^{\,n},$$
$$A_\varphi = -\alpha_2 R_{*\lambda}^{\,n} + \alpha_1 R_{*\varphi}^{\,n},$$

where $R_{*\lambda}^{\,n}$ and $R_{*\varphi}^{\,n}$ are known quantities of momentum equations at the n-th time step and α_1 and α_2 describe the change of orientation of a vector at departure point as seen at arrival point [16].

Using (3) to eliminate D^{n+1} from (4), we obtain a single equation for Φ' to be solved at each timestep.

One can see that our discretized potential vorticity equation differs from that of [5]. In particular, we use unmodified potential vorticity equation, while in [5] it was found necessary to use the linearized treatment of the Coriolis parameter in this equation. We solved this problem by separating the Coriolis parameter to be estimated at the departure point from the vorticity. Then we calculate it analytically rather than interpolate it. The other particularity consists in using the modified height field (2) in the potential vorticity equation. This allows a better account of nonlinearity of the continuity equation.

The basic fourth-order compact finite-difference formula for the first derivative (Numerov's scheme) is written as

$$\frac{1}{6} \left(\frac{\partial \varphi}{\partial x} \right)_{i-1} + \frac{2}{3} \left(\frac{\partial \varphi}{\partial x} \right)_i + \frac{1}{6} \left(\frac{\partial \varphi}{\partial x} \right)_{i+1} = \frac{\varphi_{i+1} - \varphi_{i-1}}{2h} + O(h^4). \tag{5}$$

This scheme can be also obtained from the finite-element considerations on a uniform mesh (Cullen, 1973). We can see that the Numerov's scheme differs from the usual scheme in the averaging of the derivative values, which is absent in usual schemes. In general, compact schemes possess the following advantages:

- high-order accuracy on the three-point stencil (Numerov's scheme is 6 times more accurate than explicit fourth-order central differencing),

- small phase and amplitude errors.

The disadvantage of such schemes is the necessity to solve linear systems with constant tridiagonal matrices. The part of this process can be performed in advance.

The fourth-order formula for the second derivative reads

$$\frac{1}{12} \left(\frac{\partial^2 \varphi}{\partial x^2} \right)_{i-1} + \frac{10}{12} \left(\frac{\partial^2 \varphi}{\partial x^2} \right)_i + \frac{1}{12} \left(\frac{\partial^2 \varphi}{\partial x^2} \right)_{i+1} = \frac{\varphi_{i+1} - 2\varphi_i + \varphi_{i-1}}{h^2} + O(h^4). \tag{6}$$

Of course, it is expensive to implement this approach in a straightforward way in the multi-dimensional problem. We use the Fourier representation in longitudinal direction in the semi-implicit solver replacing compact finite differences in this direction by their Fourier images. This allows to apply easily fourth-order compact finite differences on an unstaggered grid (6) and (7) to discretize first- and second-order derivatives everywhere except for the poles resulting in the same type of tridiagonal linear system for each longitudinal wavenumber as for second-order central differences. This means that the computational overhead due to high-order approximation is relatively small. The Fourier representation in longitude also facilitates the inclusion of the implicit fourth-order diffusion implemented as in [15] using 2×2 block-tridiagonal inversion in latitude.

Let us consider the discretization of the operator $\mathcal{L}$ in Eq. (4). First we rewrite the formula (7) for the second derivative of some function f with respect to λ as

$$M\left(\frac{\partial^2 f}{\partial \lambda^2}\right) = \triangle_2 f, \tag{7}$$

M being tridiagonal matrix with the elements $(1/12, 10/12, 1/12)$.

Expanding f in Fourier series in longitudinal direction, we can rewrite (7) for each Fourier harmonic $\hat{f}_k$ as

$$\frac{\partial^2 \hat{f}_k}{\partial \lambda^2} \approx -\langle k^2 \rangle \hat{f}_k,$$

where $\langle k^2 \rangle$ approximates k^2 and is the Fourier image of the operator $M^{-1}\triangle_2$,

$$\langle k^2 \rangle = \frac{\sin^2(k\triangle\lambda)}{\triangle\lambda^2(1 - 1/3 \sin^2(k\triangle\lambda/2))},$$

$\triangle\lambda$ is the mesh size in longitudinal direction. Similarly, $\partial/\partial\lambda$ is approximated by

$$\frac{\partial \hat{f}_k}{\partial \lambda} \approx -i\langle k \rangle \hat{f}_k,$$

$$\langle k \rangle = \frac{\sin(k\triangle\lambda)}{\triangle\lambda(1 - 2/3 \sin^2(k\triangle\lambda/2))}$$

and $i = \sqrt{-1}$.

Finally the discretization of the operator L in (4) for each harmonic $\hat{f}_k$ with exception for the pole points is obtained by discretizing

$$\frac{1}{a^2 \cos\varphi} \frac{\partial}{\partial\varphi} \left(g \cos\varphi \frac{\partial}{\partial\varphi} \right)$$

as

$$\frac{g_{j+1/2} \cos\varphi_{j+1/2}(\hat{f}_{k\,j+1} - \hat{f}_{k\,j}) - g_{j-1/2} \cos\varphi_{j-1/2}(\hat{f}_{k\,j} - \hat{f}_{k\,j-1})}{a^2 \cos\varphi \triangle\varphi^2}$$

and multiplying all other terms of the operator by $Ma^2 \cos\varphi$. The result is

$$a^2 \cos\varphi \left\langle \mathcal{L}\left(\hat{f}_k\right) \right\rangle = -\langle k^2 \rangle \times$$

$$\times \left(\frac{g_{j-1/2}}{24 \cos\varphi_{j-1/2}} \hat{f}_{k\,j-1} + \frac{22}{48} \frac{(g_{j-1/2} + g_{j+1/2})}{\cos\varphi_j} \hat{f}_{k\,j} + \frac{g_{j+1/2}}{24 \cos\varphi_{j+1/2}} \hat{f}_{k\,j+1} \right) -$$

$$-i\langle k\rangle\left(\frac{1}{12}\frac{\partial(gF)}{\partial\varphi}_{j-1}\hat{f}_{k\,j-1}+\frac{10}{12}\frac{\partial(gF)}{\partial\varphi}_{j}\hat{f}_{k\,j}+\frac{1}{12}\frac{\partial(gF)}{\partial\varphi}_{j+1}\hat{f}_{k\,j+1}\right)+$$

$$+\frac{g_{j+1/2}\cos\varphi_{j+1/2}(\hat{f}_{k\,j+1}-\hat{f}_{k\,j})-g_{j-1/2}\cos\varphi_{j-1/2}(\hat{f}_{k\,j}-\hat{f}_{k\,j-1})}{\triangle\varphi^2}. \tag{8}$$

Here we have to approximate $g/\cos\varphi$ in the first term of the operator L as an average between adjacent grid points to preserve the symmetry of the discretized Laplacian.

Other terms in the discretized form of (4) are also multiplied by $Ma^2\cos\varphi$ to obtain the fourth-order discretization.

At the poles, the integral approach described in [2] is used to obtain the second order discretization valid at these points. We make use of the fact that the scalar field Φ' can have only zeroth Fourier coefficient not equal to zero at the poles. The resulting tridiagonal matrix equation with complex unknowns is solved for each $\hat{\Phi}'_k$ using usual tridiagonal Gauss elimination.

Once Φ' is known, the divergence D is calculated from (4). This was found to give much less noisy field than straightforward use of (3). Next step is to obtain $\tilde{\Phi}^{n+1}$ and then relative vorticity ζ^{n+1} from (2) and (1) respectively. Now the pair of Poisson equations on the sphere is solved to find the streamfunction ψ and velocity potential χ:

$$\nabla^2\psi=\zeta, \tag{9}$$

$$\nabla^2\chi=D. \tag{10}$$

The discretization of these equations is based on the same approach as for solving (4). The only difference is that for the existence of the solution we have to fulfil the condition that the global mean of the right hand sides be zero. This is readily achieved by subtracting these global mean values from the respective right hand sides (see [1] for details).

Finally the horizontal velocity components u and v are restored using Helmholtz theorem:

$$u=-\frac{1}{a}\frac{\partial\psi}{\partial\varphi}+\frac{1}{a\cos\varphi}\frac{\partial\chi}{\partial\lambda}, \tag{11}$$

$$v=\frac{1}{a\cos\varphi}\frac{\partial\psi}{\partial\lambda}+\frac{1}{a}\frac{\partial\chi}{\partial\varphi}. \tag{12}$$

We use Numerov's scheme to discretize these derivatives.

It may seem that the proposed fourth-order algorithm for elliptic-type equations is much more complicated than the one based on second-order differences. However, as we precompute all quantities that do not change in time to solve (4) and (9 - 10), our approach requires only 3 additional arithmetic operations per equation and grid point to apply $Ma^2\cos\varphi$ to the respective right hand side terms. However, there is an additional cost in applying the fourth-order compact differencing to (11-12).

In semi-Lagrangian advection part Hermite interpolation with fifth-order compact differencing (CUD-5) derivatives estimates [21] is used to calculate the quantities at departure points of trajectories. The algorithm for finding the departure points of trajectories is described in [16]. We use linear interpolations to estimate extrapolated velocities and nonlinear term of the continuity equation at the midpoints of trajectories.

Table 1: l_2 and l_∞ error norms

Order	$ERR_2 u$	$ERR_\infty u$	$ERR_2 v$	$ERR_\infty v$
second	0.0264	0.057	0.0562	0.11
fourth	0.00932	0.018	0.00861	0.018

3 Numerical results for shallow-water version

First the model problem of restoring velocities from known vorticity and divergence using Helmholtz theorem was considered (Eqs. (9 - 12)). The velocity field to be restored is the initial velocity of the Rossby-Haurwitz wave number 4 [22]:

$$u = a\omega \cos\varphi \Big(1 + \cos^2\varphi(4\sin^2\varphi - \cos^2\varphi)\cos 4\lambda\Big),$$

$$v = -4a\omega \cos^3\varphi \sin\varphi \sin 4\lambda$$

and the associated vorticity and divergence are

$$\zeta = \omega \sin\varphi \Big(2 - 30\cos^4\varphi \cos 4\lambda\Big),$$

$$D = 0,$$
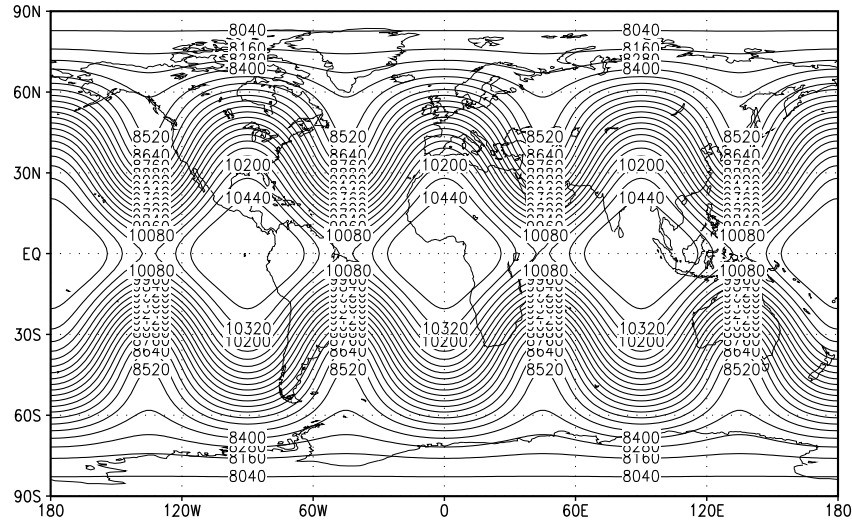
where $\omega = 7.848 \times 10^{-6}$.

Figure 1: Rossby-Haurwitz wave initial state.

Table 1 presents the l_2 and l_∞ error norms of u and v for the conventional second order and fourth-order compact finite-difference solvers with the resolution 2 degrees in longitude and latitude. As expected, the fourth-order compact finite-difference approach was found to be more accurate than second-order finite differences.
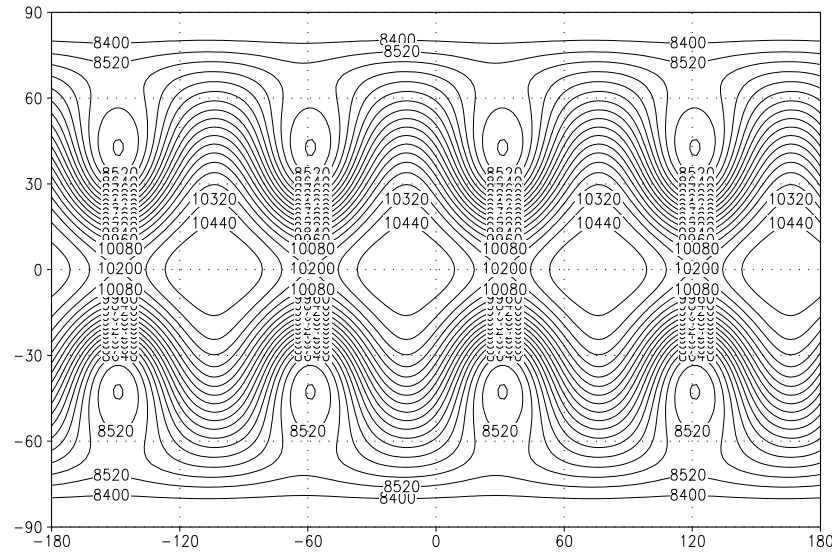
Figure 2: Evolution of Rossby-Haurwitz wave after 7-day integration.

Further tests were conducted with the 2D version of the model with the resolution 2 degrees in longitude and latitude and the time step 1 hour. The digital filter initialization [13] with the cutoff period 6 hours was applied in all cases. The standard polar numerics test and Rossby-Haurwitz wave number 4 test described in [4] were successfully passed by the model. The model was found to maintain the initial shape of Rossby-Haurwitz wave for at least one month. The initial wave and its shape after seven and 14 days of model integration are shown in Figs. 1-3 respectively. See [6] for a discussion about shape of Rossby-Haurwitz wave in different models.
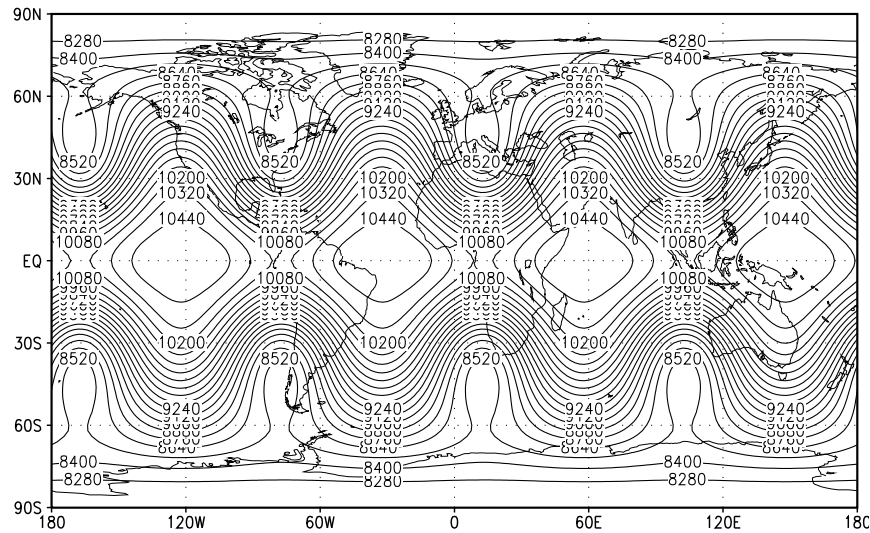

Figure 3: Evolution of Rossby-Haurwitz wave after 14-day integration.

The three real data shallow-water tests without orography from [22] were carried out. The global normalized RMS errors for the height field with respect to the high-resolution (T213) spectral Eulerian model solution [23] are given in Fig. 4a. We see that these errors are not worse

than these of solutions obtained with spectral Eulerian model with a little bit higher equivalent resolution (T63, 1.875 degrees) and the time step four times smaller ([23], Fig. 5.11).

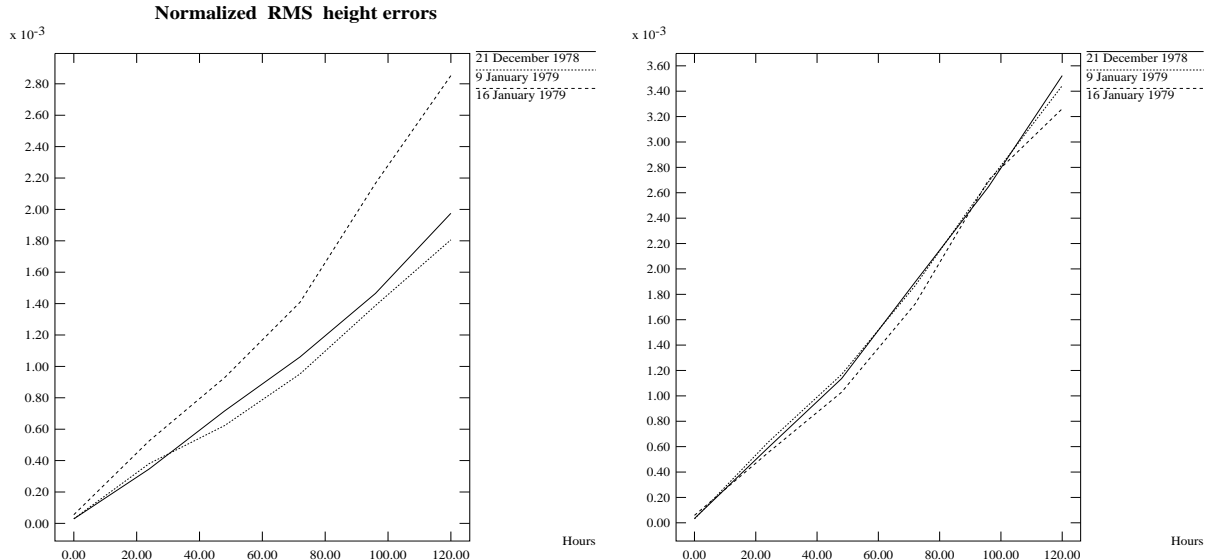**Normalized RMS height errors**

Figure 4: The global normalized RMS errors of the height field as functions of the forecast time. Hermite CUD-5 interpolation (first-order decentering parameter $\epsilon = 0.01$, horizontal diffusion coefficient $K_D = 5 \times 10^{13} \mathrm{m}^4/\mathrm{s}$, $\bar{\Phi} = 10^4$ m) (left); the same but for cubic Lagrangian interpolation (right).

For comparison, we also present RMS errors for these cases obtained with our semi-Lagrangian model but using conventional cubic Lagrangian interpolation to estimate departure point quantities (Fig. 4b). One can see that these errors are greater in the case of cubic Lagrangian interpolation. Further analysis has shown that the most significant response to the change of interpolation is observed in the discrete potential vorticity equation while other equations are sensitive to the type of interpolation to a smaller extent.

It is interesting to note the straightforward use of Φ^{n+1} instead of $\tilde{\Phi}^{n+1}$ (2) in the potential vorticity equation (1) results in a growth of errors which is 8 % on average on the fifth day.

For one of these cases, namely for the initial data of 0000 UTC 21 December 1978 we also present the initial height field, the reference solution of T213 model and the solution given by our model (Fig. 5).

Fig. 6 shows the geopotential field on the second day for the initial data of 12 February 1979 for the version with the orography. The resolution was 1.2 degrees and time step 1.5 hours, the orography was taken from [19] and the value of decentering parameter ϵ in momentum and continuity equations was 0.25, the potential vorticity equation being centered in time. We observe that spurious orographic resonance is well suppressed without degrading the accuracy of the solution (see [19] for discussion and reference solution).

The behaviour of global invariants was studied in the two months simulation with 2 degrees resolution starting from 21 December 1978 real data without orography. The relative change of mass during the period of integration was 0.04 %. The total energy after weak oscillations during first 10 days decreases with a small rate while the potential enstrophy steadily decreases starting from the beginning of the run, the values of total energy and potential enstrophy after two months being about 8 % less than initial values. In the absence of orographic forcing, the dissipation included in the model (due to interpolation and parametrized diffusion) must lead to a decay of total energy and potential vorticity.
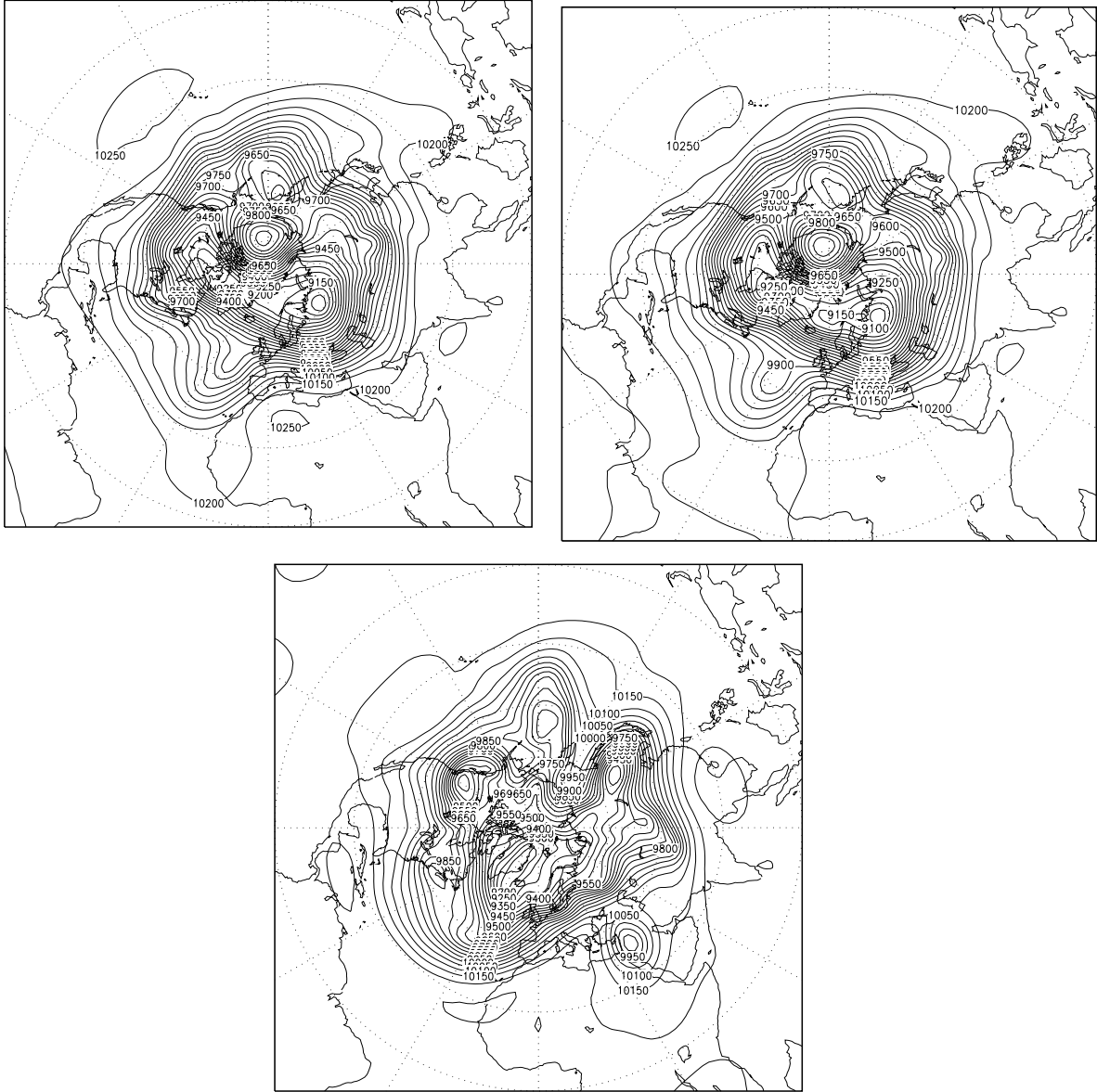
Figure 5: Reference high-resolution solution at the fifth day (left) , solution of the model on the fifth day (right) and the initial field (below) for 21 December 1978 case. Decentering parameter $\epsilon = 0.01$, diffusion coefficient $K_D = 5 \times 10^{13} \mathrm{m}^4/\mathrm{s}$.
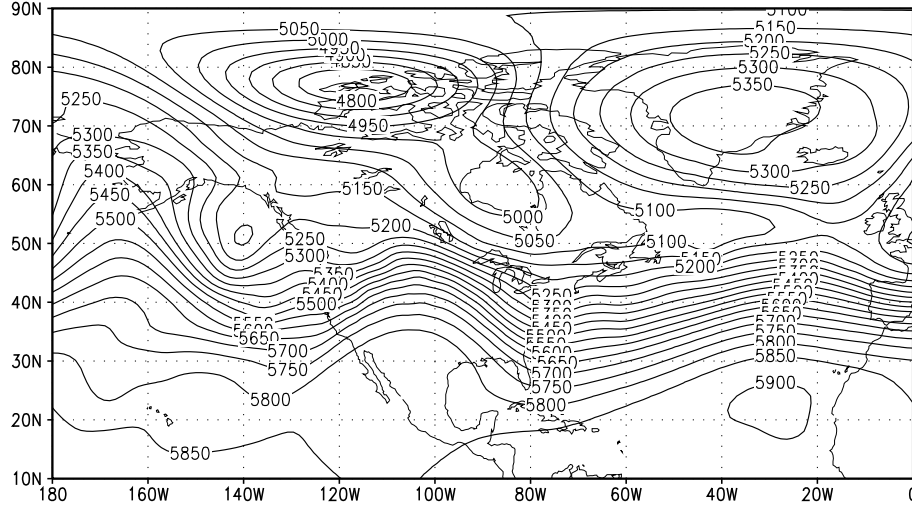
Figure 6: The part of the global 48 hours forecast height field from the initial data 12 February 1979, orography included (first-order decentering parameter $\epsilon = 0.2$, horizontal diffusion coefficient $K_D = 1 \times 10^{15} \mathrm{m}^4/\mathrm{s}$).

4   Three-dimensional model

The governing equations for the moist atmosphere are written in the vertical σ-coordinate ($\sigma = p/p_s$, where p_s is the surface pressure). The absolute vorticity is used as a prognostic variable rather than potential vorticity, keeping in mind that the latter is very difficult to use with σ vertical coordinate. Later, with the introduction of the hybrid $\sigma - \theta$ coordinate, we plan to switch to the potential vorticity equation.

The equation of absolute vorticity (see, for example, [12])

$$\frac{d}{dt}\left(\zeta + f\right) = -(\zeta + f)D - \frac{R_d}{a^2 \cos\varphi}\left(\frac{\partial T_v}{\partial \lambda}\frac{\partial \ln p_s}{\partial \varphi} - \frac{\partial T_v}{\partial \varphi}\frac{\partial \ln p_s}{\partial \lambda}\right) -$$

$$-\frac{1}{a\cos\varphi}\left(\frac{\partial \dot{\sigma}}{\partial \lambda}\frac{\partial v}{\partial \sigma} - \cos\varphi\frac{\partial \dot{\sigma}}{\partial \varphi}\frac{\partial u}{\partial \sigma}\right) + F_\zeta. \tag{13}$$

Horizontal momentum equations (used to produce discrete divergence equation)

$$\left(\frac{d\mathbf{V}}{dt}\right)_H = -\nabla\Phi - R_d T_v \nabla \ln p_s - f\mathbf{k} \times \mathbf{V} + \mathbf{F}_V, \tag{14}$$

Hydrostatic equation

$$\frac{\partial \Phi}{\partial \ln \sigma} = -R_d T_v. \tag{15}$$

Continuity equation

$$\frac{d\ln p_s}{dt} + D + \frac{\partial \dot{\sigma}}{\partial \sigma} = 0, \tag{16}$$

Thermodynamic equation

$$\frac{dT}{dt} - \frac{R_d T_v}{c_{pd}[1 + (\delta - 1)q]}\left(\frac{\dot{\sigma}}{\sigma} + \frac{d\ln p_s}{dt}\right) = F_T, \tag{17}$$

Specific humidity equation

$$\frac{dq}{dt} = F_q. \tag{18}$$

The system of equations is closed by assuming periodic boundary condition in longitude and imposing upper and lower boundary conditions

$$\dot{\sigma} = 0; \qquad \sigma = \sigma_T, 1.$$

Here p is the pressure, p_s - surface pressure, D - divergence at σ surface, R_d - dry gas constant, T - temperature, q - specific humidity, T_v - virtual temperature ($T_v = T(1 + 0.61q)$), $\kappa = R_d/c_{pd}$, c_{pd} - specific heat of dry air at constant pressure, δ - the ratio of specific heat of moist and dry air, σ_T - value of σ at the top of the model atmosphere and $\mathbf{F_V}$, F_T, F_q describe sources and sinks of momentum, heat and moisture respectively due to subgrid scale processes.

We disretize the absolute vorticity equation in time as

$$(\zeta + f)^{n+1} - (\zeta + f)^n_* = -\frac{\triangle t}{2}\Bigg[(fD)^{n+1} + (fD)^n_* +$$

$$+\left\{\zeta D + \frac{R_d}{a^2\cos\varphi}\left(\frac{\partial T}{\partial\lambda}\frac{\partial\ln p_s}{\partial\varphi} - \frac{\partial T}{\partial\varphi}\frac{\partial\ln p_s}{\partial\lambda}\right) + \frac{1}{a\cos\varphi}\left(\frac{\partial\dot{\sigma}}{\partial\lambda}\frac{\partial v}{\partial\sigma} - \cos\varphi\frac{\partial\dot{\sigma}}{\partial\varphi}\frac{\partial u}{\partial\sigma}\right)\right\}^{n+1/2} +$$

$$+\left\{\zeta D + \frac{R_d}{a^2\cos\varphi}\left(\frac{\partial T}{\partial\lambda}\frac{\partial\ln p_s}{\partial\varphi} - \frac{\partial T}{\partial\varphi}\frac{\partial\ln p_s}{\partial\lambda}\right) + \frac{1}{a\cos\varphi}\left(\frac{\partial\dot{\sigma}}{\partial\lambda}\frac{\partial v}{\partial\sigma} - \cos\varphi\frac{\partial\dot{\sigma}}{\partial\varphi}\frac{\partial u}{\partial\sigma}\right)\right\}^{n+1/2}_*\Bigg] + \triangle t F_\zeta. \tag{19}$$

Here we have used, as in the discretization of the 2D model, a centered time approximation, while other equations use first-order time uncentering to suppress the spurious orographic resonance.

Other equations are discretized in time as in [4].

$$\left(\frac{\mathbf{V}^{n+1} - \mathbf{V}^n}{\triangle t}\right)_H = -\left(\frac{1+\epsilon}{2}\left(\nabla G + f\mathbf{k}\times\mathbf{V}\right)^{n+1} + \frac{1-\epsilon}{2}\left(\nabla G + f\mathbf{k}\times\mathbf{V}\right)^n_*\right) +$$

$$+\frac{1+\epsilon}{2}(\mathbf{N}_V)^{n+1/2} + \frac{1-\epsilon}{2}(\mathbf{N}_V)^{n+1/2}_* + \mathbf{F}_V, \tag{20}$$

$$G = \Phi + R\bar{T}\ln p_s,$$

$$\mathbf{N}_V = -\nabla\Phi^w - RT'\nabla(\ln p_s),$$

$$\Phi^w_k = R_d\sum_{j=k}^{\hat{}}(T_v - T)_j\triangle\ln\sigma_j,$$

$\bar{T} = \bar{T}(\sigma)$ is the reference temperature profile and $T' = T - \bar{T}$.

$$\frac{\ln(p_s)^{n+1} - \ln(p_s)^n_{*2}}{dt} = -\frac{1+\epsilon}{2}\left(D + \frac{\partial\dot{\sigma}}{\partial\sigma}\right)^{n+1} - \frac{1-\epsilon}{2}\left(D + \frac{\partial\dot{\sigma}}{\partial\sigma}\right)^n_{*2} \tag{21}$$

$$\frac{1}{\triangle t}\left[\left(\frac{T}{\bar{T}} - \kappa\ln(p_s)\right)^{n+1} - \left(\frac{T}{\bar{T}} - \kappa\ln(p_s)\right)^n_*\right] =$$

$$\frac{1}{2}\left[(1+\epsilon)(\Gamma\dot{\sigma})^{n+1} + (1-\epsilon)(\Gamma\dot{\sigma})^n\right] + \frac{1+\epsilon}{2}(N_T)^{n+1/2} + \frac{1-\epsilon}{2}(N_T)^{n+1/2}_* + F_T, \tag{22}$$

where

$$\Gamma = \frac{\kappa}{\sigma} - \frac{1}{\bar{T}}\frac{d\bar{T}}{d\sigma},$$

$$N_T = \frac{1}{\bar{T}}\left[\dot{\sigma}\Gamma - \kappa\left(D + \frac{\partial\dot{\sigma}}{\partial\sigma}\right)\right]\left(\frac{T_v}{1 + (\delta - 1)q} - \bar{T}\right).$$

Finally, the specific humidity equation is discretized as

$$q^{n+1} = (q + F_q\triangle t)^n_* \tag{23}$$

Here $(\ )^{n+1}$ denotes a value at an arrival point at the new time level, $(\ )^n_*$ is a value at the corresponding departure point (determined by a 3D trajectory), and $(\ )^n_{*2}$ – a value at the corresponding "departure" point (determined by the horizontal projection of the 3D trajectory) at the old time level. The subscript H in (20) denotes a horizontal projection of the vector quantities.

Horizontal discretization of the above equations is based on the same compact finite differences as in 2D version. However, a care is taken to obtain consistent discretization of nonlinear terms in Eqs. (20) on a unstaggered horizontal grid. It is well known that the straightforward approximation of these terms would lead to nonlinear instability (in the case of $\mathbf{N}_V$ also to false representation of the orographic forcing). Basically, we follow the "pseudostaggering" approach proposed in [7], using fourth-order compact differences for derivatives and second-order averages. For example, the part of $\mathbf{N}_V$ term for u-component is discretized as follows:

$$\left[T'_v\frac{\partial\ln p_s}{\partial\lambda}\right]_{ij} = \frac{1}{4}\left((T'_{vi-1,j} + T'_{vij})A_\lambda^{-1}\delta_\lambda\ln p_{s_{i-1/2,j}} + (T'_{vi+1,j} + T'_{vij})A_\lambda^{-1}\delta_\lambda\ln p_{s_{i+1/2,j}}\right),$$

where $A^{-1}\triangle$ is a symbolic representation of the fourth order compact differencing on staggered grid and the operators A and $\triangle$ acting on some grid function f are defined as

$$A_\lambda f = \frac{1}{24}f_{i-1,j} + \frac{22}{24}f_{ij} + \frac{1}{24}f_{i+1,j},$$

$$\delta_\lambda f_{i+1/2,j} = (f_{i+1,j} - f_{ij})/\triangle x,$$

$$A_\varphi f = \frac{1}{24}f_{i,j-1} + \frac{22}{24}f_{ij} + \frac{1}{24}f_{i,j+1},$$

$$\delta_\varphi f_{i,j+1/2} = (f_{i,j+1} - f_{ij})/\triangle x,$$

Vertical discretization. We use staggered Lorenz grid in σ coordinate, so that all variables except for vertical velocity $\dot{\sigma}$ are defined at full levels k and $\dot{\sigma}$ is defined at half levels $k + 1/2$. The values of σ and $\dot{\sigma}$ at full level are computed as

$$\sigma_k = \frac{\sigma_{k-1/2} + \sigma_{k+1/2}}{2},$$

$$\dot{\sigma}_k = \frac{\dot{\sigma}_{k-1/2} + \dot{\sigma}_{k+1/2}}{2},$$

and

$$\triangle\ln\sigma_k = \ln(\sigma_{k+1/2}/\sigma_{k-1/2}), \qquad \triangle\sigma_k = \sigma_{k+1/2} - \sigma_{k-1/2}.$$

This gives the following expression for geopotential Φ at the vertical level k:

$$\Phi_k = \frac{1}{2} R_d T_k \triangle \ln \sigma_k \text{ if } k = NLEV,$$

$$\Phi_k = \frac{1}{2} R_d T_k \triangle \ln \sigma_k + R_d \sum_{k'=k+1}^{NLEV} T_{k'} \triangle \ln \sigma_{k'} \equiv R_d \overset{\wedge}{\underset{k}{\sum}} T_k \triangle \ln \sigma_k, \quad 1 \le k < NLEV,$$

The vertical velocity at the time level n is obtained from the diagnostic relation which is similar to the ECMWF model formulation [18], [11]:

$$\dot{\sigma}_{k+1/2}^n = -\frac{\sigma_{k+1/2} - \sigma_T}{1 - \sigma_T} \left(\frac{\partial \ln p_s}{\partial t} \right)^n - \sum_{j=1}^{k} \left[D_j + \mathbf{V}_j \cdot \nabla \ln p_s \right]^n \triangle \sigma, \tag{24}$$

where

$$\left(\frac{\partial \ln p_s}{\partial t} \right)^n = - \sum_{j=1}^{NLEV} \left[D_j + \mathbf{V}_j \cdot \nabla \ln p_s \right]^n \triangle \sigma.$$

It was shown in [4],[9] how to obtain the system of two equations for the $NLEV$ dimensional vectors of divergence $\mathbf{D}$ and generalized geopotential $\mathbf{G}$ at time level $n + 1$. First we rewrite equations at each vertical level k as

$$D_k^{n+1} + \frac{(1 + \epsilon)\triangle t}{2} \mathcal{L}(G_k^{n+1}) = \tilde{A}_k, \tag{25}$$

$$\left[\frac{T_k}{\bar{T}_k} - \kappa \ln(p_s) - \frac{(1 + \epsilon)\triangle t}{2} \Gamma_k \dot{\sigma}_k \right]^{n+1} = (B_T)_{*,k}^n + \frac{(1 + \epsilon)\triangle t}{2} (\tilde{N}_T)_k^{n+1/2} +$$

$$+ \frac{(1 - \epsilon)\triangle t}{2} (\tilde{N}_T)_{*,k}^{n+1/2}, \quad 1 \le k \le NLEV, \tag{26}$$

where

$$B_T = \frac{T}{\bar{T}} - \kappa \ln(p_s) - \frac{(1 - \epsilon)\triangle t}{2} \Gamma \dot{\sigma},$$

$$(1 - \sigma_T) \ln p_s^{n+1} + \frac{(1 + \epsilon)\triangle t}{2} \sum_{k'=1}^{NLEV} D_{k'}^{n+1} \triangle \sigma_{k'} = \sum_{k'=1}^{NLEV} (B_L)_{*2,k'}^n \triangle \sigma_{k'}, \tag{27}$$

where

$$B_L = \ln p_s - \frac{(1 - \epsilon)\triangle t}{2} \left(D + \frac{\partial \dot{\sigma}}{\partial \sigma} \right),$$

$$\frac{(1 + \epsilon)\triangle t}{2} \dot{\sigma}_{k+1/2}^{n+1} = -\left((\sigma_{k+1/2} - \sigma_T) \ln p_s + \frac{(1 + \epsilon)\triangle t}{2} \sum_{k'=1}^{k} D_{k'} \triangle \sigma_{k'} \right)^{n+1} +$$

$$+ \sum_{k'=1}^{k} (B_L)_{*2,k'}^n \triangle \sigma_{k'}, \quad 1 \le k \le NLEV - 1, \tag{28}$$

$$G_k^{n+1} = \Phi_s + R_d \overset{\wedge}{\underset{k}{\sum}} (T^{n+1} \triangle \ln \sigma)_{k'} + R_d \bar{T}_k \ln p_s^{n+1}, \quad 1 \le k \le NLEV. \tag{29}$$

We use (26), (27) and (28) to eliminate $(T_k, \ln p_s, \dot{\sigma}_{k+1/2})^{n+1}$ from (29), giving

$$G_k^{n+1} + \frac{(1 + \epsilon)\triangle t}{2} \sum_{k'=1}^{NLEV} M_{kk'} D_k^{n+1} = H_k; \quad 1 \le k \le NLEV. \tag{30}$$

The $M_{kk'}$ are functions of the standard temperature profile $\bar{T}(\sigma)$ and of the vertical discretization increments $\triangle \sigma_k$, $\triangle \ln \sigma_k$ and the H_k are known quantities given by

$$H_k = \Phi_s + R_d \sum_k \hat{\bar{T}}_{k'} \Big[(B_T)_*^n + + \frac{(1 + \epsilon)\triangle t}{2}(\tilde{N}_T)^{n+1/2} +$$

$$+\frac{(1 - \epsilon)\triangle t}{2}(\tilde{N}_T)_*^{n+1/2}\Big]_{k'} \triangle \ln \sigma_{k'} + \sum_{k'=1}^{NLEV} M_{kk'}(B_L)_{*2,k'}^n.$$

Finally we arrive to the system of two equations for $NLEV$-dimensional vectors which can be conveniently written in the matrix form as

$$\mathbf{D} + \frac{(1 + \epsilon)\triangle t}{2}\mathcal{L}(\mathbf{G}) = \tilde{\mathbf{A}}, \tag{31}$$

$$\mathbf{G} + \frac{(1 + \epsilon)\triangle t}{2}\mathbf{MD} = \mathbf{H}. \tag{32}$$

Here $\mathcal{L}$ and $\tilde{A}$ are operators defined in Eqs. (4), $\mathbf{M}$ is a $NLEV \times NLEV$ matrix with the elements $M_{kk'}$. After diagonalising linear transformation applied to matrix M, the resulting Helmholtz-type equations to be solved at each time step at each vertical level have the same form as (4) (see [4] for details).

We use trilinear interpolations at midpoints of trajectories for extrapolated velocities necessary to find trajectories. At the departure points, we use tridimensional tensor product interpolation which combines Hermite CUD-5 interpolation [21] in horizontal planes and cubic Lagrangian interpolation in the vertical direction. There is also an option in the model to use the so called non-interpolating scheme in the vertical [17], but this option was not used in the experiments described below.
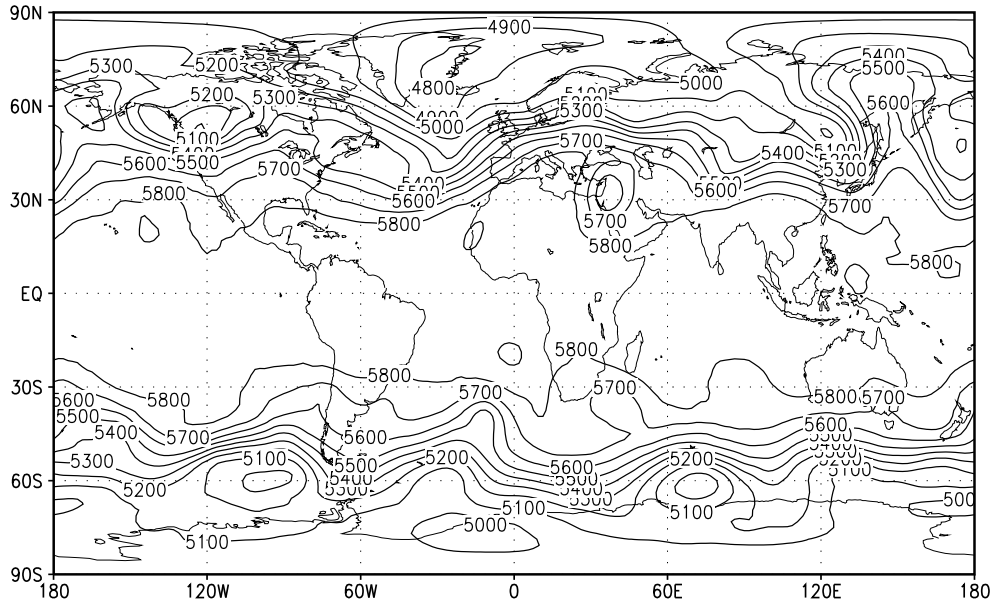

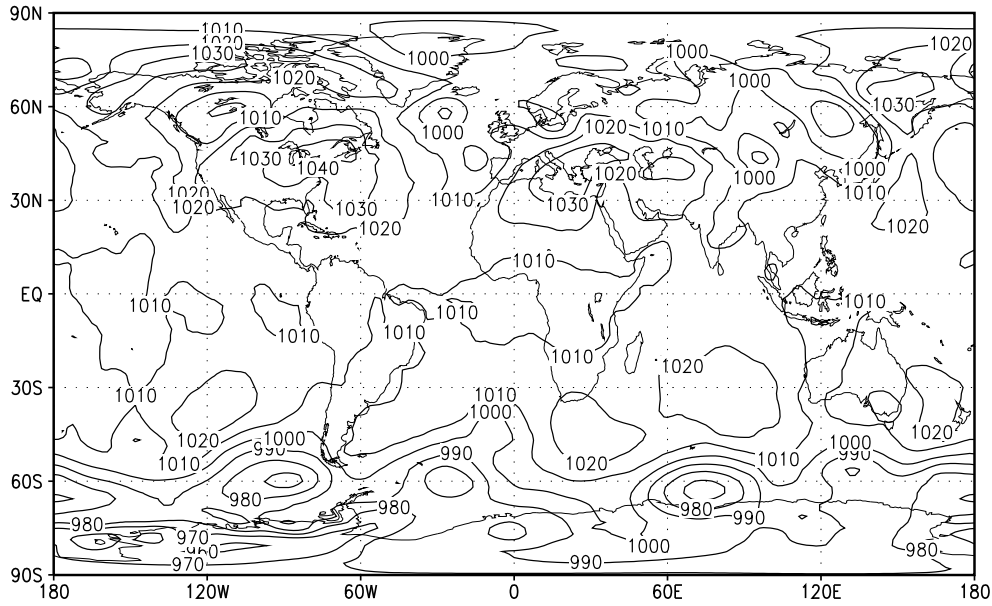Figure 7: Analyzed 500 hPa surface height for 0000UTC 21 December 1978.

Figure 8: Analyzed sea-level pressure for 0000UTC 21 December 1978.

The model includes the parametrizations of subgrid-scale processes (dry and moist convection, planetary boundary layer, shortwave and longwave solar radiation) developed in the Institute of Numerical Mathematics, Russian Academy of Sciences. For the moment being, physical parametrizations are plugged into the model using time-split approach, i.e. after each dynamical time step the fields are updated with the output tendencies of parametrizations. The radiation parametrization is called each three hours, but its tendencies are used at each time step. Also, the vertical diffusion parametrization (which was developed, as other parametrizations used, for Eulerian model) is called twice during each time step.

5 Test of the 3D model

The model was tested with the real data analysis of 0000 UTC 21 December 1978 by the European Centre for Medium-Range Weather Forecasts. The initial fields of 500 hPa height mean sea-level pressure are presented in Figs. 7, 8. This real data case caused difficulty in the developing early semi-Lagrangian model since there is a strong flow over the Northern pole [16].

The resolution was 2.5 degrees in longitude, 1.98 degrees in latitude and 16 irregularly spaced σ-levels and the time step was equal to one hour. The unusual resolution in latitude is explained by the desire to have good load balance in parallel computations. Initial condition of the model were obtained with the help of diabatic digital filter initialization [14] with the cut-off period of 6 hours.

Given the quality of initial data for horizontal velocities in high latitudes (not shown) and model resolution, we cannot expect a good forecast, but we can verify if the model demonstrates realistic behaviour.

The model was integrated for one month. The value σ_T was 0.0005 and the reference temperature profile was taken constant $\bar{T}(\sigma) = 280$ K. The forecasted field of 500 hPa height
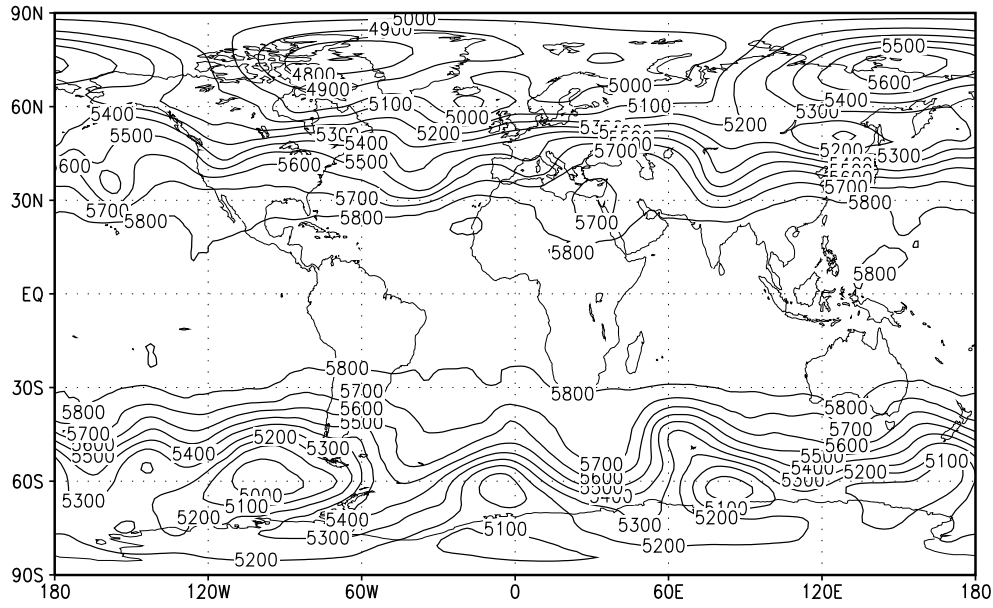
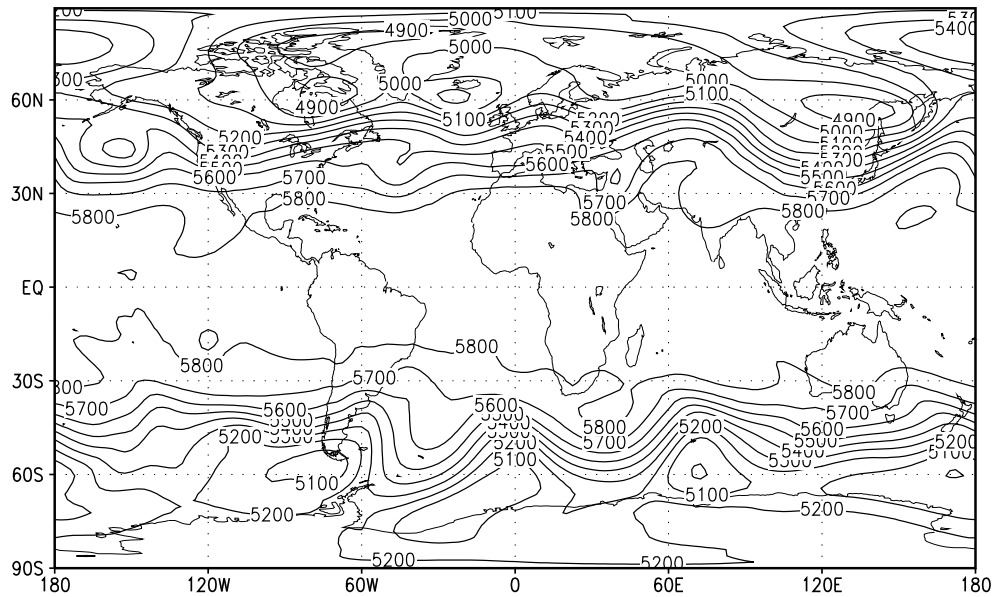Figure 9: Analyzed 500 hPa surface height for 0000UTC 24 December 1978.

Figure 10: Forecasted 500 hPa surface height for 0000UTC 24 December 1978.

after 72 hours of integration is shown in Fig. 9, while the analyzed field of the corresponding date is depicted in Fig. 10. The forecasted and analyzed mean sea-level pressure field is depicted in Figs. 11 and 12 respectively. We can see that apart form high latitudes the model gives realistic field of 500 hPa height, while surface pressure forecast is not so good. This is explained (at least partially) by the fact that the model currently uses quite crude climatological surface fields (surface temperature, sea-land mask etc.) interpolated from the model with twice coarser
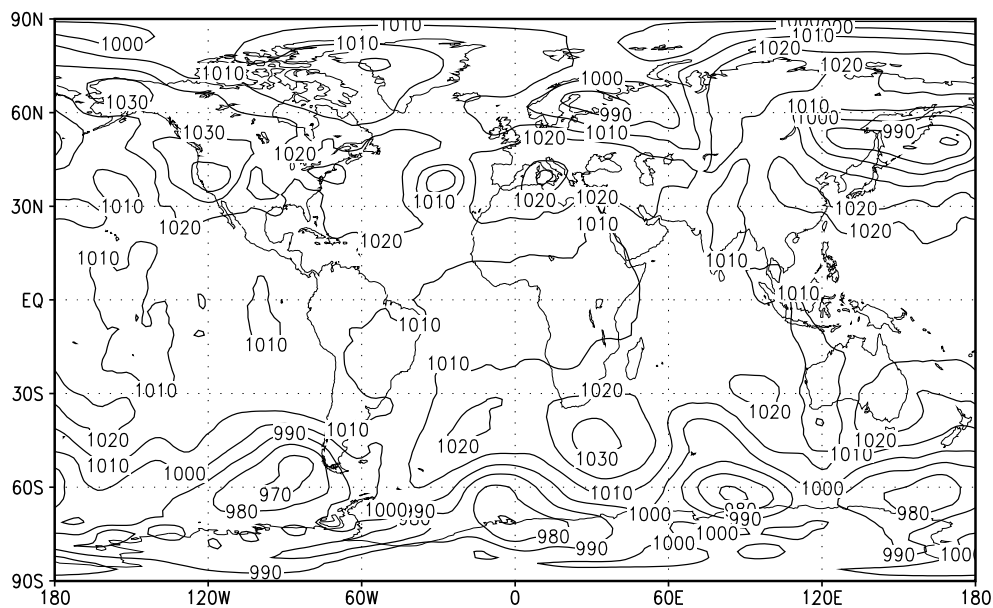
Figure 11: Analyzed sea-level pressure for 0000UTC 24 December 1978.
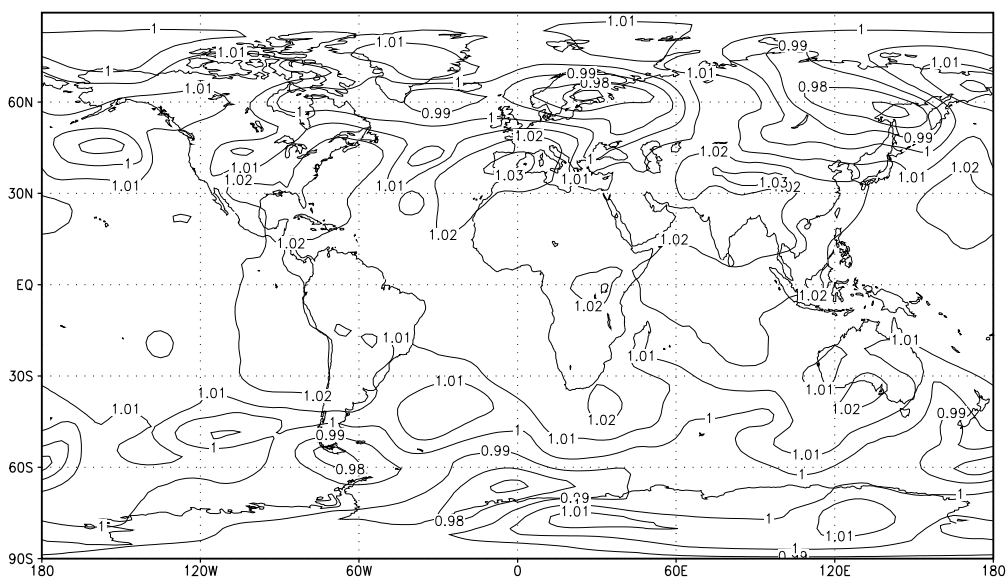

Figure 12: Forecasted sea-level pressure for 0000UTC 24 December 1978.

resolution. This will be corrected in the future version of the model. However, the pressure field is free of noise.

The relative change of the mass of the atmosphere during one month integration was less than 0.02 %.

Of course, more tests are needed, including climate simulation for at least 10 years. This would require the increase of the vertical resolution to at least 21 level to prevent the smoothing of the tropopause [8] and more realistic parametrizations of the subgrid-scale processes. Such tests are very expensive so the parallelization of the model becomes a crucial issue.

6   Parallel implementation

The code is written in Fortran 77 with the Fortran 90 extensions available in many compilers. There is an option to use the main routine written in Fortran 90 which allocates dynamically the necessary parts of big arrays depending on number of processors used. The current version of the model comprises about 30000 Fortran lines in 250 routines.

The parallelization strategy of the model assumes the distributed memory architecture. The MPI (Message Passing Interface) [10] is used to handle communications between processors. Besides being portable to many computer systems with both distributed and shared memory, MPI has an advantage to allow the communications to overlap computations. Everywhere when possible such asynchronous communications (`MPI_Isend, MPI_Irecv`) are used. We use the single program – multiple data (SPMD) approach with the master process also carrying out I/O and some additional computations.
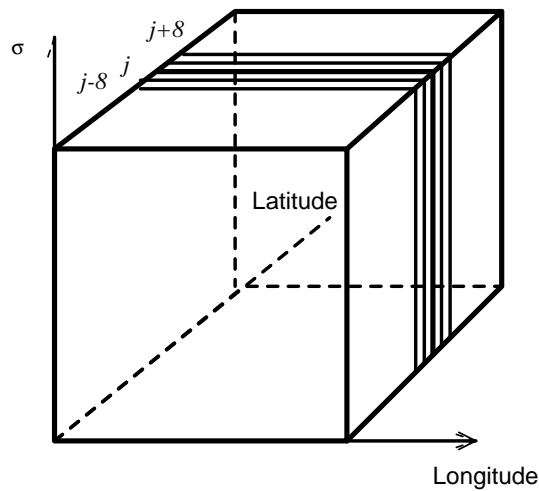

Figure 13: Domain partition in the grid-point computations.

Let us consider the computational structure of the model. First the right hand sides of equations (19-23) are computed. This includes the calculation of prognostic variables tendencies due to parametrizations (terms $\mathbf{F_V}, F_T, F_q$ and F_ζ) and calculation of terms at time levels n and $n + 1/2$ in dynamics equations. Here we have high degree of parallelism, since these computations for a given grid point do not require adjacent grid points in longitudinal and latitudinal directions, only vertical columns are needed (with a small exception for the calculation of nonlinear term $\mathbf{N_V}$). One should note that these computations represent about half of all computations in terms of the CPU time.

The next step is to find departure points and interpolate the right hand sides to them. This part is responsible for about 30 % of CPU time per time step. The Hermite CUD-5 interpolation requires 14-point stencil in longitudinal direction and 10 point-stencil in latitudinal direction. Besides, departure points of the neighbouring arrival points do not necessary lie close to each other. Departure point can lie at several grid intervals from the arrival point. The maximum width of the dependency domain can be obtained from the mesh size, time step and maximum wind speed in the atmosphere (about 110 m/s). Typical half-width of the dependency domain in our model for given resolution is 8 points in each horizontal direction. This means that for

moderate number of processors available (10-30) and a computer with significant latency time it would be beneficial to restrict ourselves by the 1D partitioning of the computational domain so that each processor performs computations in some band of latitudes (Fig. 13). Clearly, 2D partitioning is more general and allows to use much higher number of processors. However, it also results in a greater number of exchanges between processors. We will demonstrate now that on the given computer it is beneficial to reduce the number of exchanges, while the volume of the transferred data is only secondary concern.
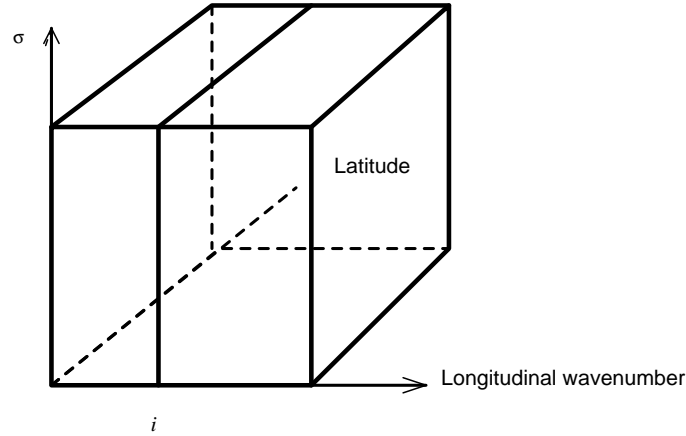
Figure 14: Domain partition in the Fourier space computations.

Indeed, before making interpolations we need to transfer the values of the computed right hand sides from adjacent latitudinal rows if these rows are computed by other processor. To interpolate quantities at departure points for one longitudinal row, we need to have data of at least 8 rows from both sides of this row. We have to transfer the data from latitudinal rows which are located in other processors. One approach to do this is to send the row once the values of the right hand sides are computed and to overlap computations of the quantities of the next row with the transfer of the already computed precedent longitudinal row. This results in a big number of exchanges. Another approach is to transfer the necessary rows after all these computations are completed. In this case the number of exchanges per processor is much smaller. The resulting parallel speedup for both strategies (in terms of the wall clock time) is depicted in Fig. 15. One can see that the second approach gives a better parallel speedup.

Once interpolations and direct fast Fourier transforms in longitude are finished, we have to redistribute data for Fourier space calculations. The calculations for each longitudinal wavenumber require the values of all latitudes (Fig. 14), so we need to provide each processor with the corresponding data. This is called data transposition. We perform it by first collecting all the data to the master processor and then sending the parts of arrays to the corresponding processors using asynchronous communications.

The computations in Fourier space involve the calculation of the RHS for the divergence equation, solution of the systems of equations (31-32), horizontal fourth-order diffusion and calculation of horizontal velocity components from Eqs. (9-12). These computations are performed in parallel for each longitudinal wavenumber. After Fourier-space calculations we need again to perform data transposition since we need all longitudinal wavenumbers to perform inverse Fourier transforms.
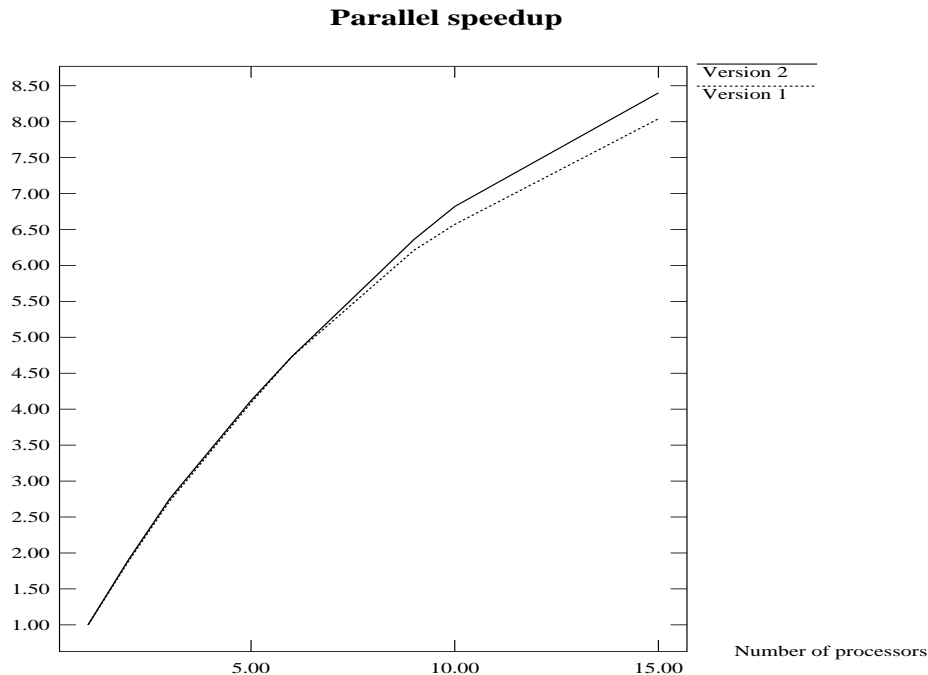
Parallel speedup

Figure 15: Comparison of two approaches for parallelization of semi-Lagrangian computations.

Practical parallel computations were conducted on Silicon Graphics Power Challenge Array. This computer has four nodes with up to 16 processors each connected via fast HIPPI crossbar. Each node has common memory for its processors. The implementation of MPI on this computer makes use of this architecture.

With the current resolution, the model can use up to 30 processors. Practical parallel computations were performed with the number of processors varying from one to 15 in the non-dedicated mode. Only numbers of processors providing good load balancing were selected. In our case, these numbers corresponding to 90 grid points at the latitudinal direction were 1, 2, 3, 5, 6, 9, 10 and 15.

Parallel speedup of our model is depicted in Fig. 16. There are two curves: for the time step with the call of solar radiation parametrization and without this call. We can observe that increasing the volume of computations in the first part of the time step results in the increased parallel efficiency. Hence one can expect that advanced (more time consuming) parametrizations of the subgrid-scale processes to be implemented in the next version of our model will improve the parallel efficiency of the code.

7   Conclusions

The global semi-Lagrangian atmospheric model based on fourth-order compact finite differences was described. The results presented for 2D shallow water version with orography demonstrate its accuracy as well as capability to maintain reasonable behaviour of global invariants. The accuracy of the shallow water version of our model verified our approach and enabled the development of the three-dimensional version. The 3D model presented here was validated using real data forecast and further one-month integration. It is considered as the first version only. However, with our experiment we demonstrated that the approach, based on fourth-order
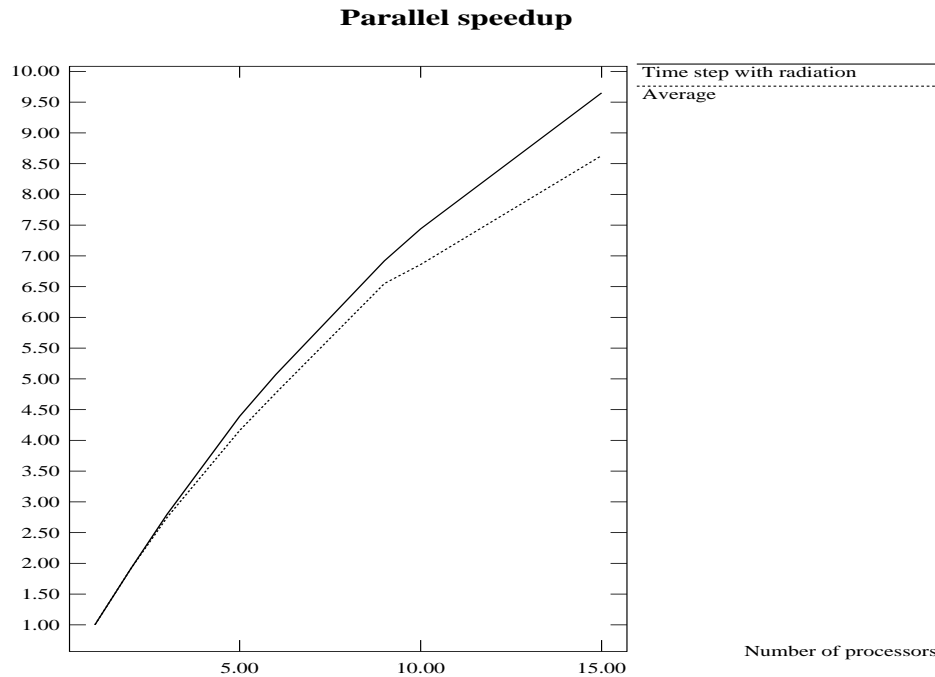
Parallel speedup

Figure 16: Comparison of parallel speedup during the time step with a call of radiation parametrization and an average speedup.

compact finite differences on unstaggered grid combined with the use of vorticity as prognostic variable, works. Further tests of the model with higher resolution are in course.

The first results of the parallel implementation on the Silicon Graphics PCA parallel computer were presented and demonstrated reasonable parallel speedup. There is still a room for further improvement of the parallel efficiency, which will be carried out in the next version of the model in the framework of the existing code.

Future development of the model will include, among other improvements in the discrete formulation, hybrid vertical coordinate and more realistic parametrizations of subgrid scale processes.

Acknowledgements

References

[1]   S. R. M. Barros, 1991: Multigrid methods for two- and three-dimensional Poisson-type equations on the sphere, *J. Comput. Phys.* **92**, 313-348.

[2]   J. R. Bates, F. H. M. Semazzi, R. W. Higgins, and S. R. M. Barros, 1990: Integration of the shallow water equations on the sphere using a vector semi-Lagrangian scheme with a multigrid solver, *Mon. Weather Rev.* **118**, 1615-1627.

[3]   J. R. Bates and M. Chen, 1996: A comparison of climate simulations from a semi-Lagrangian and an Eulerian GCM, *J. of Climate* **9**, 1126-1149.

[4]   J. R. Bates, S. Moorthi, R. W. Higgins, 1993: A global multilevel atmospheric model using a vector semi-Lagrangian finite-difference scheme, *Mon. Weather Rev.* **121**, 244-263.

[5]   J. R. Bates *et al.*, 1995: A global shallow-water numerical model based on the semi-Lagrangian advection of potential vorticity, *Quart. J. Roy. Met. Soc.* **121**, 1981-2006.

[6]   Yong Li and J. R. Bates, 1996: A study of the behavior of semi-Lagrangian models in the presence of orography, *Quart. J. Roy. Met. Soc.* **122**, 1675-1700.

[7]   J. Côtê, S. Gravel and A. Staniforth, 1990: Improving variable-resolution finite-element semi-Lagrangian integration schemes by pseudostaggering, *Mon. Weather Rev.* **118**, 2718-2731.

[8]   *Proceedings of ECMWF workshop on semi-Lagrangian methods 6-8.11.1995*, 1996: ECMWF, Reading, UK, 3-10.

[9]   A. McDonald, J. Haugen, 1992: A two-time-level, three-dimensional semi-Lagrangian, semi-implicit, limited-area gridpoint model of the primitive equations, *Mon. Weather Rev.* **120**, 2603-2621.

[10]   Gropps *et al*, 1995: Using MPI

[11]   N. Gustafsson and A. McDonald, 1996: A comparison of the HIRLAM gridpoint and spectral semi-Lagrangian model, *Mon. Weather Rev.* **124**, 2008-2022.

[12]   J. R. Holton, 1979: *An introduction to dynamic meteorology*, Academic Press.

[13]   P. Lynch and X.-Y. Huang, 1992: Initialization of the HIRLAM model using a digital filter, *Mon. Weather Rev.* **120**, 1019-1034.

[14]   X.-Y. Huang and P. Lynch, 1993: Diabatic digital-filtering initialization: Application to the HIRLAM model, *Mon. Weather Rev.* **121**, 589-603.

[15]   Yong Li, S. Moorthi, J. R. Bates, 1994: Direct solution of the implicit formulation of fourth order horizontal diffusion for gridpoint models on the sphere, *NASA GLA Technical report series in atmospheric modelling and data assimilation, Vol. 2.*

[16]   H. Ritchie, 1988: Application of the semi-Lagrangian method to a spectral model of the shallow-water equations, *Mon. Weather Rev.* **116**, 1587-1598.

[17]   H. Ritchie, 1991: Application of the semi-Lagrangian method to a multi-level spectral primitive-equations model, *Quart. J. Roy. Met. Soc.* **117**, 91-106.

[18]   H. Ritchie, C. Temperton, A. Simmons, M. Hortal, T. Davies, D. Dent and M. Hamrud, 1995: Implementation of the semi-Lagrangian method in a high resolution version of the ECMWF forecast model. *Mon. Weather Rev.*, **123**, 489-514.

[19]   Ch. Rivest, A. Staniforth, A. Robert, 1994: Spurious resonant response of semi-Lagrangian discretizations to orographic forcing: diagnosis and solution, *Mon. Weather Rev.* **122**, 366-376.

[20]   M. Tanguay, E. Yakimiw, H. Ritchie, A. Robert, 1992: Advantages of spatial averaging in semi-implicit semi-Lagrangian schemes, *Mon. Weather Rev.* **120**, 113-123.

[21]   M. Tolstykh, 1995: The response of the variable resolution semi-Lagrangian NWP model to the change of horizontal interpolation, accepted to *Quart. J. Roy. Met. Soc.*

[22]   D. L. Williamson *et al.*, 1992: A standard test set for numerical approximations to the shallow water equations in spherical geometry, *J. Comput. Phys.*, **102**, 211-224.

[23]   R. Jakob-Chien, J. J. Hack, D. L. Williamson, 1995: Spectral transform solutions to the shallow water test set,*J. Comput. Phys.*, **119**, 164-187.

[24]   D. L. Williamson and J. G. Olson, 1994: Climate simulatoin with a semi-Lagrangian version of the NCAR Community Climate Model, *Mon. Weather Rev.* **122**, 1594-1610.